ELECTROCHEMISTRY

Homogeneously dispersed multimetal oxygen-evolving catalysts

Bo Zhang,[1,2]* Xueli Zheng,[1,3]* Oleksandr Voznyy,[1]* Riccardo Comin,[1] Michal Bajdich,[4,5] Max García-Melchor,[4,5] Lili Han,[3,6] Jixian Xu,[1] Min Liu,[1] Lirong Zheng,[7] F. Pelayo García de Arquer,[1] Cao Thang Dinh,[1] Fengjia Fan,[1] Mingjian Yuan,[1] Emre Yassitepe,[1] Ning Chen,[8] Tom Regier,[8] Pengfei Liu,[9] Yuhang Li,[9] Phil De Luna,[1] Alyf Janmohamed,[1] Huolin L. Xin,[6] Huagui Yang,[9] Aleksandra Vojvodic,[4,5]† Edward H. Sargent[1]†

Earth-abundant first-row (3d) transition metal–based catalysts have been developed for the oxygen-evolution reaction (OER); however, they operate at overpotentials substantially above thermodynamic requirements. Density functional theory suggested that non-3d high-valency metals such as tungsten can modulate 3d metal oxides, providing near-optimal adsorption energies for OER intermediates. We developed a room-temperature synthesis to produce gelled oxyhydroxides materials with an atomically homogeneous metal distribution. These gelled FeCoW oxyhydroxides exhibit the lowest overpotential (191 millivolts) reported at 10 milliamperes per square centimeter in alkaline electrolyte. The catalyst shows no evidence of degradation after more than 500 hours of operation. X-ray absorption and computational studies reveal a synergistic interplay between tungsten, iron, and cobalt in producing a favorable local coordination environment and electronic structure that enhance the energetics for OER.

Efficient, cost-effective, and long-lived electrolysers are a crucial missing piece along the path to fuels synthesized with renewable electricity (*1*, *2*). The bottleneck in improving water-splitting technologies is the oxygen-evolving reaction (OER), in which even the most efficient precious-metal catalysts require a substantial overpotential (η) to reach the desired current densities of ≥10 mA cm^{-2} (*2*, *3*). Researchers have explored earth-abundant first-row (3d) transition-metal oxides (*4*–*9*), including 3d metal oxyhydroxides (*4*, *5*), oxide perovskites (*7*), cobalt phosphate composites (*6*), nickel borate composites (*10*), and molecular complexes (*9*, *11*). The OER performance of multimetal oxides based on iron (Fe), cobalt (Co), and nickel (Ni) is particularly promising, and OER activity often outperforms that of the corresponding single-metal oxides (*5*, *12*–*15*).

[1]Department of Electrical and Computer Engineering, University of Toronto, 35 St George Street, Toronto, Ontario M5S 1A4, Canada. [2]Department of Physics, East China University of Science and Technology, 130 Meilong Road, Shanghai 200237, China. [3]Tianjin Key Laboratory of Composite and Functional Materials, School of Materials Science and Engineering, Tianjin University, Tianjin 300072, China. [4]SUNCAT Center for Interface Science and Catalysis, Department of Chemical Engineering, Stanford University, Stanford, CA 94305, USA. [5]SLAC National Accelerator Laboratory, 2575 Sand Hill Road, Menlo Park, CA 94025, USA. [6]Center for Functional Nanomaterials, Brookhaven National Laboratory, Upton, New York 11973, USA. [7]Beijing Synchrotron Radiation Facility, Institute of High Energy Physics, Chinese Academy of Sciences, Beijing 100049, China. [8]Canadian Light Source (CLS), 44 Innovation Boulevard, Saskatoon, SK, S7N 2V3, Canada. [9]Key Laboratory for Ultrafine Materials of Ministry of Education, School of Materials Science and Engineering, East China University of Science and Technology, 130 Meilong Road, Shanghai 200237, China. *These authors contributed equally to this work. †Corresponding author. E-mail: ted.sargent@utoronto.ca (E.H.S); alevoj@stanford.edu (A.V.)

We examined whether multimetal oxide OER catalysts could be improved by systematically modulating their 3d electronic structure. Prior results suggest that the introduction of additional metals has a limited impact on the behavior of the 3d metals, likely because of their undesired separation into two noninteracting metal oxide phases (*16*, *17*). For modulation, we focus in particular on tungsten (W), which in its highest oxidation state is a structurally versatile coordination host (*9*, *11*). We began with computational studies aimed at identifying effects of W-modulation of the local coordination environment and the impacts on the resulting electronic structure and on the consequent energetics of the OER. The OER performance of unary Co, Fe, and Ni oxides has been well established both from theory and experiment (*14*, *15*, *18*). Previous computational studies show that the OER activity is mainly driven by the energetics of the OER intermediates (*OH, *O, and *OOH) on the surfaces, with the O to OH adsorption energy difference being the main descriptor for the observed activity trends among these materials (*14*, *15*, *18*). Binary metal oxides such as Ni-Fe and Co-Fe, as well as doped unary oxides, have also been investigated, and their activity can also be predicted by using the above-mentioned descriptor-based approach (*5*, *12*, *13*). Theoretical studies suggest that for a given unary metal oxide, the energetics of OER intermediates can be modulated by incorporating metal elements, and that in turn these tune the catalytic activity of these materials.

Theoretical calculations of ternary and higher mixtures of oxides have been hindered by the complexity of these materials and the associated computational cost. We simplified our approach by starting from the calculated OER energetics for the pure β-CoOOH, γ-FeOOH, and WO_3 phases and estimating the effect of alloying on the energetics of OER intermediates via simple linear interpolation arguments. Our density functional theory plus U (DFT+U) calculations revealed that the adsorption energy of OH is too strong on the FeOOH(010) surface, whereas it is too weak on the CoOOH(01-12) and WO_3(001) surfaces (Fig. 1A) (*19*). To test the interpolation principle, we next calculated the OH adsorption energy on the Fe-doped CoOOH(01-12) surface: This energy falls approximately halfway between the one obtained for the unary CoOOH(01-12) and FeOOH(010) surfaces. Similarly, adding Co into WO_3(001) or adding W into CoOOH(01-12) led to an averaged OH adsorption energy for the $CoWO_4$ system (*20*) and W-doped CoOOH(01-12). By extending this scheme to ternary Co-Fe-W metal-oxide systems, we estimate that FeW-doped CoOOH(01-12) should result in near-optimal *OH energetics for OER.

Next, we proceeded to calculate the energetics of all intermediates (*OH, *O, and *OOH) and extracted overpotentials for the set of unary and Fe- and W-doped surfaces mentioned above [computational methodology is provided (*19*)]. Given the plethora of possible ternary Co-Fe-W oxide alloys, we limited our computational study to the investigation of the above active site motifs, which are also expected to benefit from the interpolation scheme of Fig. 1A. We chose to study only the chemistry of substitutionally metal-doped surface sites. All calculated theoretical OER overpotentials shown in the two-dimensional (2D) volcano plot of Fig. 1B support the general validity of the interpolation scheme not just for *OH energetics, but also for the O to OH adsorption energy difference, denoted as ΔG_O-ΔG_{OH}. The potential limiting kinetic barriers for the reaction were also experimentally determined and found to be small compared with thermodynamics (*19*). The tunability of adsorption energies upon alloying would hence allow for substantial improvement in OER activity.

We found that the OER activity of the unary pure CoOOH(01-12) surface can be improved via single-site doping with subsurface Fe atoms. This improvement can be attributed to the change in ΔG_{OH} and also in ΔG_O-ΔG_{OH} at the Co-site and can be rationalized by the difference in electron affinity between Co^{4+} (at the surface) and Fe^{3+} (subsurface) sites. Furthermore, adding a W dopant in the vicinity of the Co active site of the Fe-doped CoOOH surface (Fig. 1B, inset) further improves the energetics for OER. The substitution of a W dopant at a Co^{4+} site results in (i) migration of protons away from W, which prefers the W^{6+} formal oxidation state, toward oxygen at Co sites, and (ii) compressive strain of larger W atoms on the surrounding Co sites. As a result of these geometric and electronic changes, we identified a favorable direct O_2 mechanism for OER with a theoretical overpotential of only 0.4 V compared with the standard electrochemical OOH mechanism [computational methodology details are provided in (*19*)].

In light of these findings, we sought to devise a controlled process to incorporate W^{6+} into FeCo

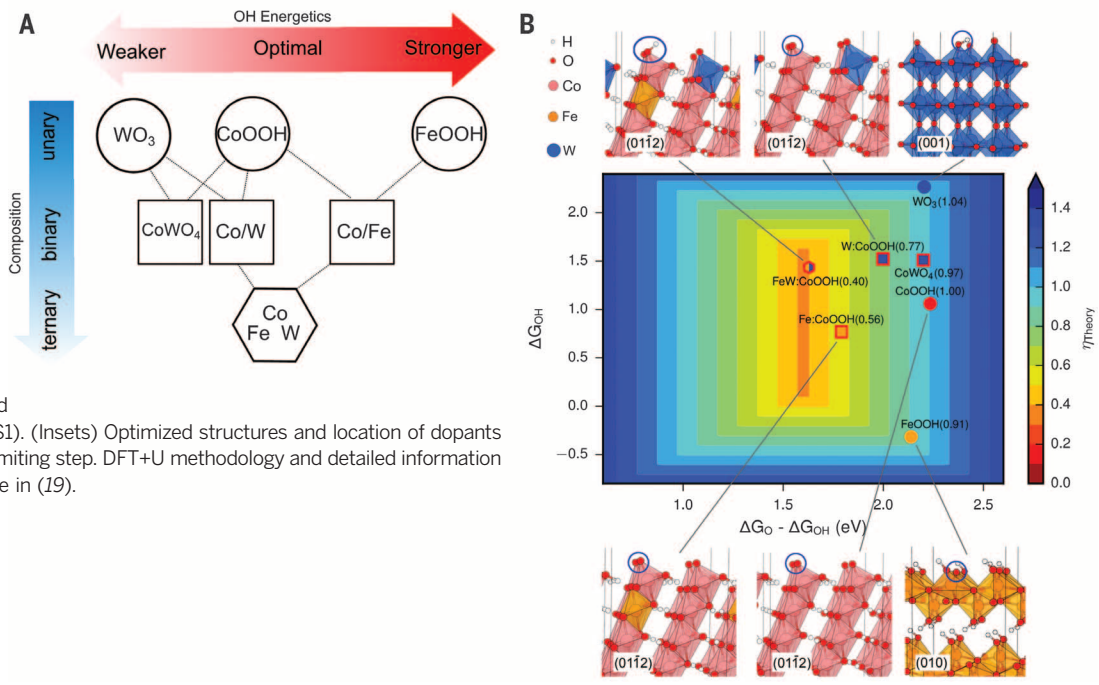

Fig. 1. Tuning the energetics of OER intermediates via alloying. (**A**) Change in OH adsorption energetics (ΔG_{OH}) as a function of increasing composition obtained by interpolation between the calculated pure phases: WO_3 (001), CoOOH (01-12), FeOOH (010), and $CoWO_4$ (010) (*20*). (**B**) OER activities of pure Fe,Co oxyhydroxides and W,Fe-doped Co oxyhydroxides, cobalt tungstate, and W oxides calculated with DFT+U. The optimum is obtained for WFe-doped β-CoOOH (table S1). (Insets) Optimized structures and location of dopants and active sites at the potential limiting step. DFT+U methodology and detailed information about these systems are available in (*19*).

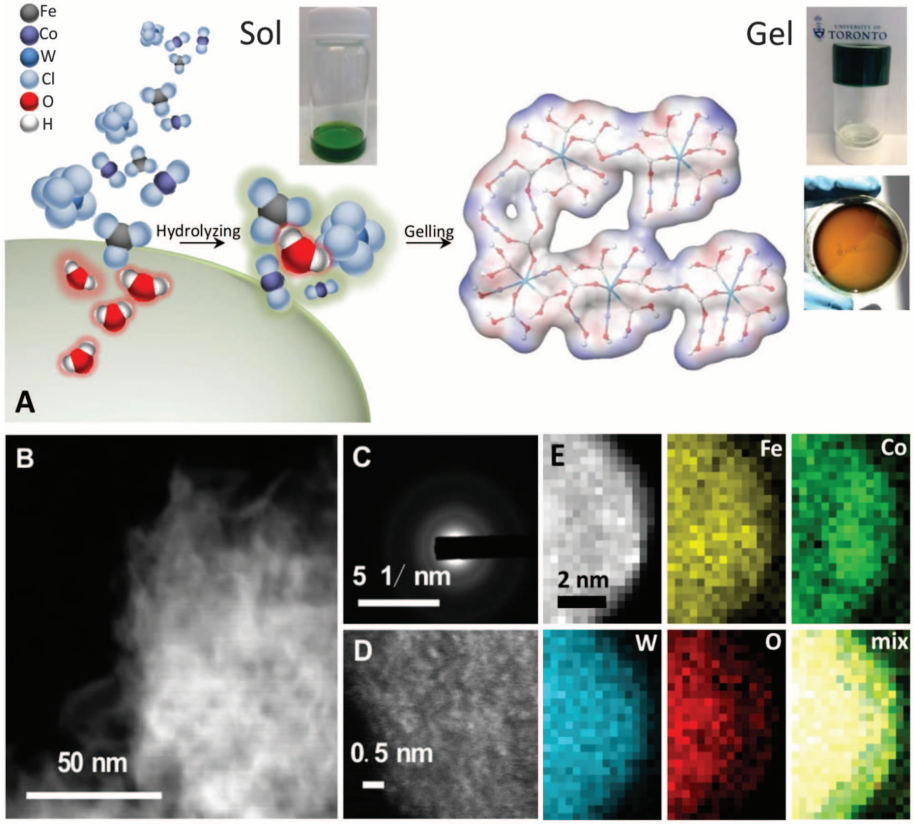

Fig. 2. Preparation of G-FeCoW oxyhydroxides catalysts. (**A**) Schematic illustration of the preparation process for the gelled structure and pictures of the corresponding sol, gel, and gelled film. (**B**) HAADF-STEM image of nanoporous structure of G-FeCoW. (**C**) SAED pattern. (**D**) Atomic-resolution HAADF-STEM image. (**E**) EELS elemental mapping from the G-FeCoW oxyhydroxides sample.

oxyhydroxides in an atomically homogeneous manner. We explored a room-temperature sol-gel procedure that would feature precursors mixed in a homogeneous manner that would be hydrolyzed at a controlled rate so as to achieve atomic homogeneity. First, we dissolved inorganic metal chloride precursors in ethanol. These were controllably hydrolyzed in order to produce a multimetal oxyhydroxide gel via a room-temperature sol-gel process (Fig. 2A) (*21*). The hydrolysis rates of $CoCl_2$, $FeCl_3$, and WCl_6 vary greatly, so very low concentrations of water and propylene oxide were used to tune their hydrolysis independently—a strategy that we anticipated could lead to the desired homogeneous spatial distribution of the three metallic elements (*19*).

After supercritical drying with CO_2, the gel transformed into amorphous metal oxyhydroxides powders. From inductively coupled plasma optical emission spectrometry (ICP-OES) analysis, we determined the molar ratio of Fe:Co:W to be 1:1.02:0.70. Atomic-resolution scanning transmission electron microscopy (STEM) performed in high-angle annular dark field (HAADF) mode (Fig. 2D and fig. S5A), combined with selected-area electron diffraction (SAED) analysis (Fig. 2C), revealed the absence of a crystalline phase. X-ray diffraction (XRD) (fig. S2A) further confirmed that the gelled FeCoW is an amorphous phase (*19*). The STEM measurements show a crumpled and entangled structure composed of nanosheets and nanopores (Fig. 2B). Electron energy loss spectroscopy (EELS) elemental maps with sub-nanometer resolution (Fig. 2E) showed a uniform, uncorrelated spatial distribution of Fe, Co, and W. The statistics of the atom-pair separation distances, obtained from the STEM elemental maps, show that the nearest-neighbor separations of all

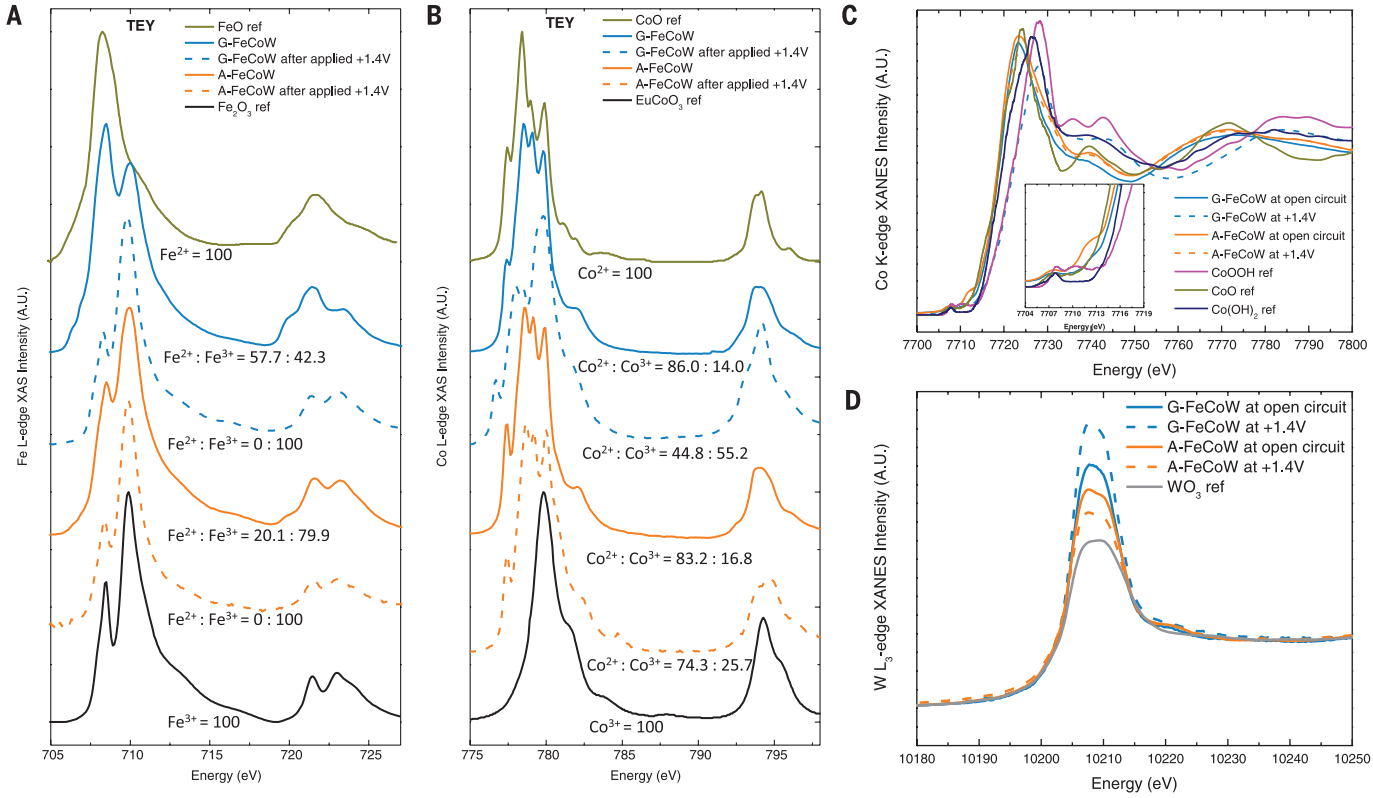

Fig. 3. Surface and bulk x-ray absorption spectra of G-FeCoW oxyhydroxide catalysts and A-FeCoW controls. (**A**) Surface-sensitive TEY XAS scans at the Fe L-edge before and after OER at +1.4 V (versus RHE), with the corresponding molar ratio of Fe^{2+} and Fe^{3+} species. (**B**) Surface-sensitive TEY XAS scans at the Co L-edge before and after OER at +1.4 V (versus RHE). (**C**) Bulk Co K-edge XANES spectra before and after OER at +1.4 V (versus RHE). (Inset) The zoomed in pre-edge profiles. The Co K-edge data of $Co(OH)_2$ and CoOOH are from (*30*). (**D**) Bulk W L3-edge XANES spectra before and after OER at +1.4 V (versus RHE).

Table 1. Comparison of catalytic parameters of G-FeCoW and controls.

Samples	On gold foam	On glassy carbon electrode (GCE)		On Au(111)		References
	Overpotential* (mV)	Overpotential* (mV)	TOF† (s^{-1})	Overpotential* (mV)	ΔH (kJ mol^{-1}) at η=300 mV	
LDH FeCo	279 (±8)	331 (±3)	0.0085	429 (±4)	81	This work
G-FeCo	215 (±6)	277 (±3)	0.043	346 (±4)	60	This work
G-FeCoW	191 (±3)	223 (±2)	0.46 (±0.08)	315 (±5)	49	This work
A-FeCoW	232 (±4)	301 (±4)	0.17	405 (±2)	80	This work
Amorphous-$FeCoO_x$‡	–	300	–	–	–	(*4*)
LDH NiFe	–	300	0.07	–	–	(*25*)
CoOOH	–	–	–	550	–	(*23*)
IrO_2	–	260	0.05	–	–	(*25*)
NiFeOOH	–	340	–	–	66 (-/+5)	(*27*)
$Ni_{60}Co_{40}$ oxides	–	263	–	–	72.6§	(*29*)
NiFe LDH/ GO	–	210	0.1	–	–	(*22*)

*Obtained at the current density of 10 mA cm^{-2}, without *iR* correction. †Obtained at 95% *iR* corrected η = 300 mV, assuming all loaded 3d-metal atoms as active sites. ‡Obtained from the LSV plots at the current density of 4 mA cm^{-2} in 0.1 M KOH aqueous solution. §Obtained at 280 mV in 1M NaOH aqueous solution.

two-metal atom pairs are highly consistent (figs. S3, S4, and S6, A to E) (*19*). This homogeneity results from (i) the homogeneous dispersion of three precursors in solution and (ii) controlled hydrolysis, the latter enabling the maintenance of the homogeneous phase in the final gel state without phase separation of different metals caused by precipitation. In contrast, conventional processes (*17*), even when their precursors are homogeneously mixed, result in crystalline products formed heterogeneously during the annealing process leading to phase separation caused by lattice mismatch. For structural comparison with prior sol-gel reports that used an annealing step (*17*), we annealed the samples at 500°C and

then found crystalline phases (figs. S5B, high-resolution TEM images, and S2B, XRD) that included separated Fe_3O_4, Co_3O_4, and $CoWO_4$. Elemental mapping of this sample (fig. S6, A1 to E1) further confirmed the phase separation of Fe from Co and W atoms (*19*).

We investigated the influence of incorporating W (with its high oxidation state) on the electronic and coordination structures of Fe and Co using x-ray absorption spectroscopy (XAS). We examined (i) conventionally layered double hydroxides of FeCo (LDH FeCo) that have the same structure as the state-of-the-art OER catalysts (LDH NiFe) (*22*), (ii) FeCo oxyhydroxides (without W) prepared via the annealing-free sol-gel process (gelled FeCo, labeled G-FeCo), (iii) gelled FeCoW oxyhydroxides (G-FeCoW), and (iv) annealed G-FeCoW at 500°C (A-FeCoW).

To evaluate the change of oxidation states of metal elements during OER, we performed XAS on the G-FeCoW and A-FeCoW samples before and after OER; the latter condition was realized by oxidizing samples at +1.4 V versus the reversible hydrogen electrode (RHE) in the OER region. XAS in total electron yield (TEY) mode provides information on the near-surface chemistry (below 10 nm). We acquired TEY data at the Fe and Co L-edges on samples prepared ex situ. For comparison, on the same samples we also measured in situ XAS (during OER) at the Fe and Co K-edges via fluorescent yield, a measurement that mainly probes chemical changes in the bulk. TEY XAS spectra in Fig. 3A revealed that the surface Fe^{2+} ions in G-FeCoW had been oxidized to Fe^{3+} at +1.4 V, which is in agreement with thermodynamic data for Fe. However, the oxidation states of Co in G-FeCoW and A-FeCoW samples were appreciably different at +1.4 V. In G-FeCoW, the valence states of both surface (Fig. 3B) and bulk (Fig. 3C) Co were similar to pure Co^{3+}, including only a modest admixture with Co^{2+} (fig. S12); in particular, the Co-K edge profile closely resembled CoOOH (*23*), which is consistent with our DFT model. In contrast, in A-FeCoW (in which W is phase-separated), even after a potential of +1.4 V was applied, the surface (Fig. 3B) and bulk (Fig. 3C) manifested a substantially higher Co^{2+} content (fig. S12), which is consistent with the Co_3O_4 and $CoWO_4$ phases. These oxides had been found to be much less reactive in DFT simulations (*14*, *20*). The bulk and surface Fe and Co edge profiles are shown in figs. S7 to S11 and discussed in (*19*).

The white lines of W L_3-edge x-ray absorption near-edge structure (XANES) spectra of all samples in Fig. 3D show that W in G-FeCoW and A-FeCoW samples before and after OER has a distorted WO_6 octahedral symmetry (*24*). The W L_3 amplitude in pre-OER A-FeCoW was low, a finding attributable to the loss of bound water during annealing (*24*). When a +1.4 V bias was applied, the W L_3 intensity in G-FeCoW increased, indicating that the valence of W decreases, which is consistent with increased distortion of WO_6 octahedra (*24*). This result agrees with the results of DFT, in which W-doped CoOOH(01-12) is expected to produce W residing in a lower oxidation state. These results indicate that Fe and Co also inversely influence W in the homogeneous ternary metal oxyhydroxides.

In situ extended x-ray absorption fine structure (EXAFS) (figs. S13 and S14) on G-FeCoW showed a significant decrease in Co-O bond distance, from 2.06 to 1.91 Å, after a potential of +1.4 V was applied. This decrease is consistent with the reported results that the Co-O bond distance in CoOOH is shorter than that in $Co(OH)_2$ (*23*). EXAFS data at the Fe edge in G-FeCoW show the same trend (figs. S15 and S16). Ex situ EXAFS data before OER are also shown in figs. S17 to S20 and table S3. In contrast, the local structural arrangement in A-FeCoW remains unchanged at 1.4 V. Overall, we conclude that Co in the G-FeCoW structure is more readily oxidized to high valence, which is consistent with G-FeCoW being more active than the control annealed samples.

We compared the OER performance of our gelled sample G-FeCoW with that of the reference samples G-FeCo, LDH FeCo, and A-FeCoW. Representative OER currents of the samples were measured for spin-coated thin films (thickness ~ 30 nm) (fig. S21) (*19*) on a well-defined Au(111) single-crystal electrode (Fig. 4A) in 1 M KOH aqueous electrolyte at a scan rate of 1 mV s^{-1} (currents are uncorrected and thus include the effects of resistive losses incurred within the electrolyte). The G-FeCoW–on-Au(111) required an overpotential of only 315 mV

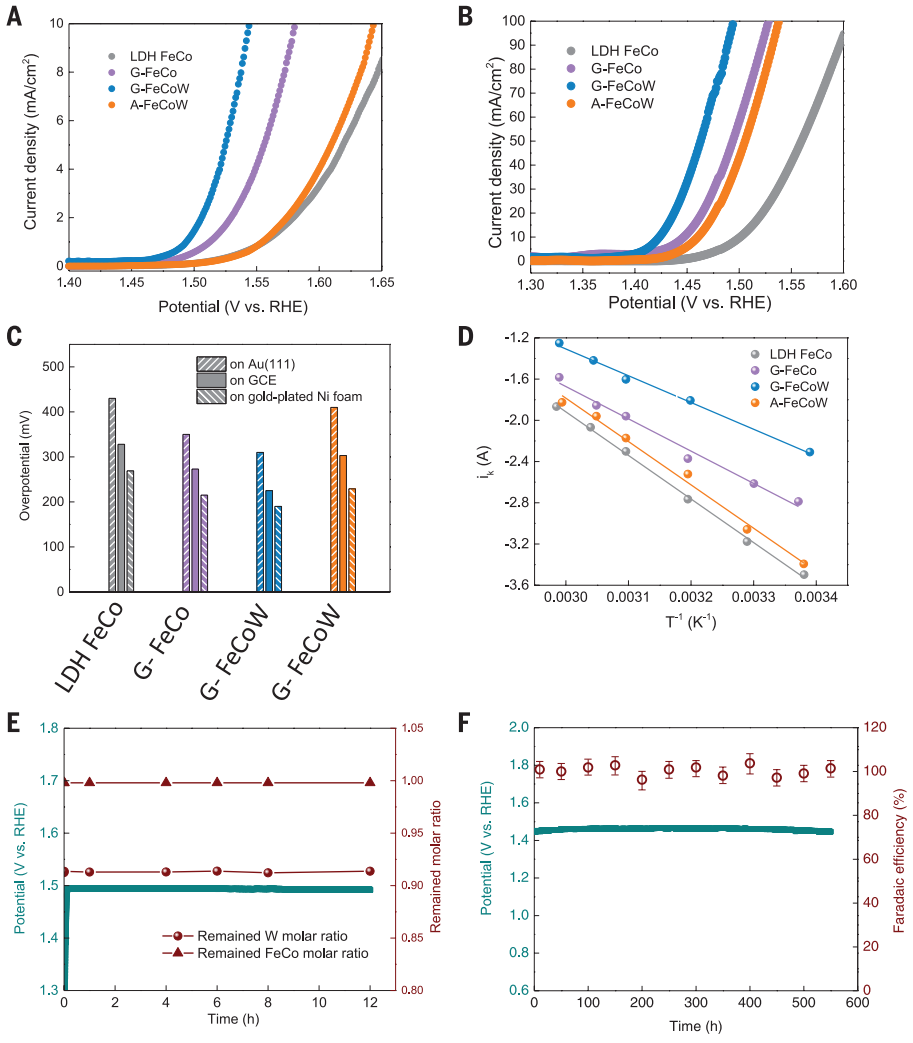

Fig. 4. Performance of G-FeCoW oxyhydroxides catalysts and controls in three-electrode configuration in 1 M KOH aqueous electrolyte. (**A** and **B**) The OER polarization curve of catalysts loaded on two different substrates with 1 mV s^{-1} scan rate, without *iR* correction: (A) Au(111) electrode and (B) gold-plated Ni foam. (**C**) Overpotentials obtained from OER polarization curves at the current density of 10 mA cm^{-2} tested on Au(111), GCE and gold-plated Ni foam, respectively, without *iR* correction. (**D**) Arrhenius plot of the kinetic current at η = 300 mV, tested on Au(111), without *iR* correction. (**E**) Chronopotentiometric curves obtained with the G-FeCoW oxyhydroxides on gold-plated Ni foam electrode with constant current densities of 30 mA cm^{-2}, and the corresponding remaining metal molar ratio in G-FeCoW calculated from ICP-AES results. (**F**) Chronopotentiometric curves obtained with the G-FeCoW oxyhydroxides on gold-plated Ni foam electrode with constant current densities of 30 mA cm^{-2}, and the corresponding Faradaic efficiency from gas chromatography measurement of evolved O_2.

at 10 mA cm^{-2} (Table 1, all current densities based on projected geometric area). This potential is 114 mV lower than that of precipitated FeCo LDH fabricated for the present study. When W was not introduced, the resultant G-FeCo gelled catalyst required an additional overpotential of 31 mV to reach a similar current density. When the gelled sample was subjected to a postsynthetic thermal treatment (500°C anneal), the overpotential of the FeCoW electrode increased to 405 mV at 10 mA cm^{-2}.

To assess the impact of the electrode support and compare the performance of the new catalysts with the state-of-the-art NiFeOOH, we tested on glassy carbon electrode (GCE) using the identical three-electrode system and with a catalyst loading mass of 0.21 mg cm^{-2}. The trend of the overpotentials remains the same (fig. S22), with the G-FeCoW–on-GCE electrode requiring an overpotential of 223 mV at 10 mA cm^{-2}. Without carbon additives, and without *iR* corrections (*i*, current; *R*, resistance), the G-FeCoW catalyst consistently outperforms the best oxide catalysts previously reported (Table 1) (*4*, *22*, *25*).

Next, we investigated whether the OER-performance of G-FeCoW originates from intrinsic catalytic activity of multimetal active sites or exclusively from an enhanced surface area. We analyzed the Brunauer-Emmett-Teller (BET) surface area, which allowed us to report normalized kinetic current density (referred to as specific activity) as a function of potential versus RHE (*7*). We confirmed that the intrinsic activity of G-FeCoW is notably higher than that of the controls and also higher than those previously reported (fig. S26) (*7*).

The intrinsic activity of G-FeCoW was further confirmed by determining the mass activities and turnover frequencies (TOFs) for this catalyst. We used data obtained on GCE with 95% *iR* correction at $\eta = 300$ mV (the remaining data in this work are not corrected by 95% *iR*, unless stated). As shown in Table 1 and tables S5 and S9 (*19*), the G-FeCoW catalysts on GCE exhibit TOFs of 0.46 s^{-1} per total 3d metal atoms and mass activities of 1175 A g^{-1} (considering the total loading mass on the lower limiting case). If only considering electrochemically active 3d metals or mass (obtained from the integration of Co redox features) (*26*), G-FeCoW catalysts exhibit much higher TOFs of 1.5 s^{-1} and 3500 A g^{-1}. These are more than three times above the TOF and mass activities of the optimized control catalysts and the repeated state-of-the-art NiFeOOH (table S9) (*5*, *26*).

To assess the kinetic barriers involved in OER, we studied the effect of temperature on the performance of the catalysts (fig. S27). OER proceeds more rapidly at elevated temperatures, reflecting the exponential temperature dependence of the chemical rate constant (*27*). The Arrhenius plots at $\eta = 300$ mV for four different catalysts (Fig. 4D) allowed us to extract electrochemical activation energies that agree well with the values reported previously (Table 1) (*27*). We found that G-FeCoW has the lowest apparent barrier value of 49 kJ mol^{-1}. The similar data obtained for all catalysts suggests that OER proceeds via the same potential-determining step on all catalysts investigated in this work.

To obtain a highly efficient catalytic electrode, we increased the conductivity of the substrate by loading our catalysts on a nickel foam that was covered with gold in order to avoid any spurious effects arising from interaction of the catalyst with Ni. The activity trends of catalysts remained the same as observed on the Au(111) surface and GCE, whereas the absolute performance of each sample was substantially improved (Fig. 4B). The G-FeCoW showed a low overpotential of 191 mV at 10 mA cm^{-2} on the gold-plated nickel foam (projected geometric area) (Table 1). On the basis of the above discussion and the overpotentials on Au(111), gold foam, GCE, and fluorine-doped tin oxide (Fig. 4C, fig. S30, and table S6), it can be seen that the catalytic activity of G-FeCoW is much higher than that of the annealed control (A-FeCoW), gelled FeCo without W (G-FeCo), and the LDH FeCo having the same structure as the state-of-the-art LDH NiFeOOH OER catalysts.

The operating stability of the OER catalysts is essential to their application (*28*). To characterize the performance stability of the G-FeCoW catalysts, we ran water oxidation on the catalyst deposited on gold-plated Ni foam under constant current of 30 mA cm^{-2} continuously for 550 hours. We observed no appreciable increase in potential in this time interval (Fig. 4, E and F). To check that the catalyst remained physically intact, we tested in situ its mass using the electrochemical quartz crystal microbalance (EQCM) technique (figs. S31 and S32) and also assessed whether any metal had leached into the electrolyte by using inductively coupled plasma atomic emission spectroscopy (ICP-AES) (figs. S33 to S36 and table S7). After the completion of an initial burn-in period in which (presumably unbound) W is shed into the electrolyte, we saw stable operation and no discernible W loss. EELS mapping of G-FeCoW after OER (fig. S37) indicates that the remaining W continues to be distributed homogeneously in the sample. By measuring the O_2 evolved from the G-FeCoW/gold-plated Ni foam catalyst, we also confirmed the high activity throughout the entire duration of stability test, obtaining quantitative (unity Faradaic efficiency) gas evolution of O_2 to within our available ±5% experimental error (Fig. 4F). These findings suggest that modulating the 3d transition in metal oxyhydroxides by using a suitable transition metal, one closely atomically coupled through homogeneous solid-state dispersion, may provide further avenues to OER optimization.

REFERENCES AND NOTES

1. C. R. Cox, J. Z. Lee, D. G. Nocera, T. Buonassisi, *Proc. Natl. Acad. Sci. U.S.A.* **111**, 14057–14061 (2014).
2. J. Luo *et al.*, *Science* **345**, 1593–1596 (2014).
3. M. Schreier *et al.*, *Nat. Commun.* **6**, 7326 (2015).
4. R. D. L. Smith *et al.*, *Science* **340**, 60–63 (2013).
5. D. Friebel *et al.*, *J. Am. Chem. Soc.* **137**, 1305–1313 (2015).
6. M. W. Kanan, D. G. Nocera, *Science* **321**, 1072–1075 (2008).
7. J. Suntivich, K. J. May, H. A. Gasteiger, J. B. Goodenough, Y. Shao-Horn, *Science* **334**, 1383–1385 (2011).
8. A. Vojvodic, J. K. Nørskov, *Science* **334**, 1355–1356 (2011).
9. Q. Yin *et al.*, *Science* **328**, 342–345 (2010).
10. M. Dincă, Y. Surendranath, D. G. Nocera, *Proc. Natl. Acad. Sci. U.S.A.* **107**, 10337–10341 (2010).
11. F. M. Toma *et al.*, *Nat. Chem.* **2**, 826–831 (2010).
12. M. S. Burke, M. G. Kast, L. Trotochaud, A. M. Smith, S. W. Boettcher, *J. Am. Chem. Soc.* **137**, 3638–3648 (2015).
13. M. W. Louie, A. T. Bell, *J. Am. Chem. Soc.* **135**, 12329–12337 (2013).
14. M. Bajdich, M. García-Mota, A. Vojvodic, J. K. Nørskov, A. T. Bell, *J. Am. Chem. Soc.* **135**, 13521–13530 (2013).
15. C. C. L. McCrory *et al.*, *J. Am. Chem. Soc.* **137**, 4347–4357 (2015).
16. J. A. Haber *et al.*, *Energy Environ. Sci.* **7**, 682–688 (2014).
17. J. A. Haber, E. Anzenburg, J. Yano, C. Kisielowski, J. M. Gregoire, *Adv. Ener. Mat.* **5**, 1402307 (2015).
18. P. Liao, J. A. Keith, E. A. Carter, *J. Am. Chem. Soc.* **134**, 13296–13309 (2012).
19. Materials and methods are available as supplementary materials on *Science* Online.
20. C. Ling, L. Q. Zhou, H. Jia, *RSC Adv.* **4**, 24692–24697 (2014).
21. V. Augustyn *et al.*, *Nat. Mater.* **12**, 518–522 (2013).
22. W. Ma *et al.*, *ACS Nano* **9**, 1977–1984 (2015).
23. R. Subbaraman *et al.*, *Nat. Mater.* **11**, 550–557 (2012).
24. A. Balerna *et al.*, *Nucl. Instrum. Methods Phys. Res. A* **308**, 240–242 (1991).
25. F. Song, X. Hu, *Nat. Commun.* **5**, 4477 (2014) .
26. A. S. Batchellor, S. W. Boettcher, *ACS Catal.* **5**, 6680–6689 (2015).
27. J. R. Swierk, S. Klaus, L. Trotochaud, A. T. Bell, T. D. Tilley, *J. Phys. Chem. C* **119**, 19022–19029 (2015).
28. N. Danilovic *et al.*, *Angew. Chem. Int. Ed. Engl.* **126**, 14240–14245 (2014).
29. F. Rosalbino, S. Delsante, G. Borzone, G. Scavino, *Int. J. Hydrogen Energy* **38**, 10170–10177 (2013).
30. D. Friebel *et al.*, *Phys. Chem. Chem. Phys.* **15**, 17460–17467 (2013).

ACKNOWLEDGMENTS

This work was supported by the Ontario Research Fund–Research Excellence Program, Natural Sciences and Engineering Research Council of Canada, and the Canadian Insititute for Advanced Research Bio-Inspired Solar Energy program. B.Z. acknowledges funding from China Scholarship Council/University of Toronto Joint Funding Program (201406745001), Shanghai Municipal Natural Science Foundation (14ZR1410200), and the National Natural Science Foundation of China (21503079). X.Z. acknowledges a scholarship from the China Scholarship Council (CSC) (20140625004). This work was also supported by the U.S. Department of Energy (DOE), Office of Basic Energy Science grant to the SUNCAT Center for Interface Science and Catalysis and the Laboratory-Directed Research and Development program funded through the SLAC National Accelerator Laboratory. M.G.-M. acknowledges funding from the Agency for Administration of University and Research Grants of Catalonia (AGAUR, 2013 BP-A 00464). This work has also benefited from the Hard X-ray Micro-Analysis and Spherical Grating Monochromator beamlines at CLS and the BL14W1 beamline at the Shanghai Synchrotron Radiation Facility (SSRF). B.Z. and R.C. acknowledge the CLS Post-Doctoral Student Travel Support Program. The TEM study in this work is supported by the Center for Functional Nanomaterials, which is a DOE Office of Science Facility, at Brookhaven National Laboratory under contract DE-SC0012704. E.Y. acknowledges a Fundação de Amparo à Pesquisa do Estado de São Paulo–Bolsa Estágio de Pesquisa no Exterior (2014/18327-9) fellowship. E.H.S. and F.P.G.A acknowledge funding from the Connaught Global Challenge program of the University of Toronto. The authors thank D. Bélanger and G. Chamoulaud at Université du Québec à Montréal for assistance in EQCM measurements and T.-O. Do and C.-C. Nguyen at Laval University for surface area analysis. The authors thank Y. J. Pang, X. Lan, L. N. Quan, and S. Hoogland for fruitful discussions; M. X. Liu and X. W. Gong for fabrication assistance; and R. Wolowiec and D. Kopilovic for assistance. B.Z., X.Z., J.X., M.L., C.T.D, and E.H.S. of the University of Toronto have filed provisional patent application no. 62288648 regarding the preparation of multimetal catalysts for oxygen evolution.

SUPPLEMENTARY MATERIALS

www.sciencemag.org/content/352/6283/333/suppl/DC1
Materials and Methods
Figs. S1 to S43
Tables S1 to S9
References (*31*–*56*)

23 December 2015; accepted 9 March 2016
10.1126/science.aaf1525

Editor's Summary

Modulating metal oxides

The more difficult step in fuel cells and water electrolysis is the oxygen evolution reaction. The search for earth-abundant materials to replace noble metals for this reaction often turns to oxides of three-dimensional metals such as iron. Zhang *et al.* show that the applied voltages needed to drive this reaction are reduced for iron-cobalt oxides by the addition of tungsten. The addition of tungsten favorably modulates the electronic structure of the oxyhydroxide. A key development is to keep the metals well mixed and avoid the formation of separate phases.

Science, this issue p. 333